Journal of Instrumentation

PAPER • **OPEN ACCESS**

Evaluation of planar silicon pixel sensors with the RD53A readout chip for the Phase-2 Upgrade of the CMS Inner Tracker

To cite this article: W. Adam *et al* 2023 *JINST* **18** P11015

Published by IOP Publishing for Sissa Medialab

Received: *July 6, 2023*
Accepted: *September 15, 2023*
Published: *November 17, 2023*

Evaluation of planar silicon pixel sensors with the RD53A readout chip for the Phase-2 Upgrade of the CMS Inner Tracker

The Tracker Group of the CMS collaboration

E-mail: georg.steinbrueck@uni-hamburg.de

Abstract: The Large Hadron Collider at CERN will undergo an upgrade in order to increase its luminosity to $7.5 \times 10^{34}\,\mathrm{cm}^{-2}\mathrm{s}^{-1}$. The increased luminosity during this High-Luminosity running phase, starting around 2029, means a higher rate of proton-proton interactions, hence a larger ionizing dose and particle fluence for the detectors. The current tracking system of the CMS experiment will be fully replaced in order to cope with the new operating conditions. Prototype planar pixel sensors for the CMS Inner Tracker with square 50 µm × 50 µm and rectangular 100 µm × 25 µm pixels read out by the RD53A chip were characterized in the lab and at the DESY-II testbeam facility in order to identify designs that meet the requirements of CMS during the High-Luminosity running phase. A spatial resolution of approximately 3.4 µm (2 µm) is obtained using the modules with 50 µm × 50 µm (100 µm × 25 µm) pixels at the optimal angle of incidence before irradiation. After irradiation to a 1 MeV neutron equivalent fluence of $\Phi_{\mathrm{eq}} = 5.3 \times 10^{15}\,\mathrm{cm}^{-2}$, a resolution of 9.4 µm is achieved at a bias voltage of 800 V using a module with 50 µm × 50 µm pixel size. All modules retain a hit efficiency in excess of 99% after irradiation to fluences up to $2.1 \times 10^{16}\,\mathrm{cm}^{-2}$. Further studies of the electrical properties of the modules, especially crosstalk, are also presented in this paper.

Keywords: Particle tracking detectors (Solid-state detectors); Radiation-hard detectors; Si microstrip and pad detectors; Large detector systems for particle and astroparticle physics

ArXiv ePrint: 2307.01580

https://doi.org/10.1088/1748-0221/18/11/P11015

2023 JINST 18 P11015

Contents

2023 JINST 18 P11015

1 Introduction

The Large Hadron Collider (LHC) at CERN will be upgraded in order to increase the instantaneous luminosity from currently $2 \times 10^{34}\,\mathrm{cm}^{-2}\,\mathrm{s}^{-1}$ to $7.5 \times 10^{34}\,\mathrm{cm}^{-2}\,\mathrm{s}^{-1}$, boosting the physics potential of its experiments [1]. An integrated luminosity of 3000 to 4000 fb^{-1} will have been delivered by the end of the 10 year High-Luminosity LHC (HL-LHC) program, which is an increase by about a factor of ten with respect to the first three runs of the LHC ending in 2025 [2]. The increased instantaneous luminosity means a higher rate of proton-proton interactions, on the order of 200 per bunch crossing, and thus a higher particle fluence and total ionizing dose (TID) in the detectors. The Compact Muon Solenoid (CMS) detector [3, 4] will be upgraded in order to maintain or even improve its measurement capabilities under such challenging conditions.

This paper focuses on the upgrade of the CMS Inner Tracker (IT) [5], which is entirely composed of silicon pixel detectors. The upgraded IT will feature a two-phase CO_2 cooling system with a liquid CO_2 temperature of $-33\,^{\circ}\mathrm{C}$, leading to sensor temperatures in the range of -20 to $-15\,^{\circ}\mathrm{C}$. A layout of the CMS IT is shown in figure 1. The IT is constructed in three parts: the Tracker Barrel Pixel Detector (TBPX), the Tracker Forward Pixel Detector (TFPX), and the Tracker Endcap Pixel Detector (TEPX). The TBPX comprises four cylindrical detector layers, while the TFPX and TEPX feature eight and four discs per side, respectively. The innermost layer of the IT barrel section will be located at a radius of 28 mm from the beam axis. Here, a non-ionizing energy loss (NIEL) corresponding to a 1 MeV neutron equivalent particle fluence of $\Phi_{\mathrm{eq}} = 3.5 \times 10^{16}\,\mathrm{cm}^{-2}$ and a total ionizing dose (TID) of 19 MGy are expected after 4000 fb^{-1} of integrated luminosity over 10 years of operation. Neither the readout chips nor the sensors are expected to be operable under these conditions and a replacement of the first

layer is foreseen part-way through the HL-LHC running period. The radial distances of all barrel layers and of the rings of the forward and endcap discs from the center of the beam pipe are reported in ref. [5].

Planar n^+-p pixel sensors with an active thickness of 150 µm will be used throughout the IT with the exception of the first layer of TBPX, where 3D sensors are the baseline choice given their intrinsically higher radiation tolerance and lower power consumption [6]. Owing to their more complicated production process, which results in a lower production yield and higher prices, 3D sensors are not an option for the entire IT.

The maximum fluence for planar sensors will be reached in ring 1 of the TFPX. For the full lifetime of the IT, with 4000 fb^{-1} delivered, the fluence in this ring is expected to reach 2.3×10^{16} cm^{-2}. This value refers to the maximum fluence, received at the inner module edge, while the mean fluence over the module is much lower, about 1.3×10^{16} cm^{-2} over the full detector lifetime. In ring 2 of TFPX and barrel layer 2, fluences of 1.1×10^{16} cm^{-2} and 9.4×10^{15} cm^{-2} are expected, respectively. The IT is constructed such that ring 1 in TFPX can be exchanged at a fluence of about 1.2×10^{16} cm^{-2} part-way through the HL-LHC period. In this case, the limiting factor for the lifetime is likely the increase in power consumption of the sensors, leading to a deterioration of the cooling performance, and ultimately thermal runaway. The CMS readout chip has been tested up to a total ionizing dose of 10 MGy. Tests at the dose level of 15 MGy, expected for the detector region equipped with planar sensors for the full detector lifetime, are planned for 2023.

Initially, pixel sizes of 50 µm × 50 µm and 100 µm × 25 µm were considered, with the long side oriented parallel to the beam axis (along z) in the barrel and radially outwards (along r) in the forward and endcap discs. In the process of evaluating pixel tracking performance, sensors with both pixel sizes were measured. Guided by tracking and physics simulations of the entire tracking system, CMS has decided to use 100 µm × 25 µm pitch sensors throughout the entire IT (including the 3D modules in barrel layer 1).

A variety of prototype pixel sensors have been designed and fabricated. These include 3D and planar sensors of both pixel sizes with p-stop or p-spray isolation and with or without a biasing scheme for sensor tests before flip-chip bump bonding [7]. The sensors evaluated in this paper are planar

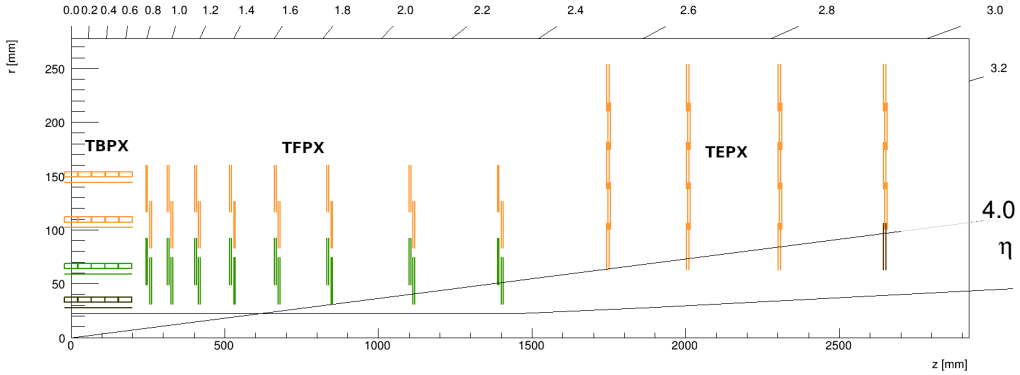

Figure 1. Layout of the CMS Inner Tracker (IT) for Phase-2. In the IT, pixel detector modules with 2 × 2 readout chips (shown in yellow) and 1 × 2 readout chips (shown in green) are used [5]. The innermost part of TBPX (shown in black) comprises 1 × 2 modules with two individual 3D sensors. The innermost ring of disc 4 of TEPX (shown in brown) consists of 2 × 2 modules and sends data to the luminosity system. The lower black line represents the outer radius of the beam pipe.

2023 JINST 18 P11015

sensors designed to match the layout of the RD53A readout chip (ROC), which is a half-size prototype of the final ROC developed by the RD53 Collaboration, a joint effort by the ATLAS and CMS Collaborations [8]. The measurements are performed using the *Linear front-end* [9] of the RD53A chip.

This paper describes studies for a variety of RD53A-sensor assemblies with the aim to evaluate their performance and to select sensor designs that meet CMS specifications. A list of selected specifications for planar pixel sensors is shown in table 1. Since tuning of the chip parameters is critical for an optimal performance of the assemblies and to obtain reliable results, a significant part of the paper is devoted to this aspect.

The pixel modules studied in this paper are described in section 2. In section 3, the tuning procedure and performance of the RD53A-sensor assemblies are described. Laboratory measurements of crosstalk in these modules are reported in section 4. Evaluation of the sensors with particle beams and the results are discussed in section 5.

Table 1. Selected requirements for planar pixel sensors used for this measurement and vendor qualification campaign. The requirements for the procurement of sensors for the final experiment differ slightly. The full depletion voltage and the hit efficiency are denoted by V_{depl} and ϵ_{hit}, respectively.

Parameter	Value	Measured at
polarity	n^+-p	
active thickness	150 µm	
bulk resistivity	3 kΩcm to 20 kΩcm	room temperature
pixel size	50 µm × 50 µm 100 µm × 25 µm	
breakdown voltage before irradiation	> 300 V	
breakdown voltage after $\Phi_{\text{eq}} = 5 \times 10^{15}\,\text{cm}^{-2}$	> 800 V	
leakage current before irradiation	< 0.75 µA cm^{-2}	at V_{depl} + 50 V at 20 °C
leakage current after $\Phi_{\text{eq}} = 5 \times 10^{15}\,\text{cm}^{-2}$ annealing at 60 °C for 1 hr	< 45 µA cm^{-2}	at 600 V at −25 °C
ϵ_{hit} before irradiation	> 99%	V_{depl} + 50 V
ϵ_{hit} for $\Phi_{\text{eq}} = 5 \times 10^{15}\,\text{cm}^{-2}$	> 99%	≤ 800 V, −20 °C
ϵ_{hit} for $\Phi_{\text{eq}} = 1 \times 10^{16}\,\text{cm}^{-2}$	> 98%	≤ 800 V, −20 °C

2 Pixel modules

A pixel module consists of a silicon pixel sensor bump bonded to one or more readout chips to form a hybrid pixel detector. In this study, only single-chip modules are tested. The baseline choice for the three outer barrel layers and the discs of the IT are fine-pitch n^+-p planar pixel sensors with an active thickness of 150 µm. The layouts of the investigated sensor cells are displayed in figure 2 together with the definition of the local x and y sensor coordinates used in this paper.

2023 JINST 18 P11015

Sensors with and without a punch-through bias dot [10] are evaluated. The dot enables the biasing of the sensor for testing before bump bonding to a readout chip. This makes it possible to identify sensors with low breakdown voltages through current-voltage measurements before the non-reversible bump bonding process. The prototype sensors discussed in this paper were produced by Hamamatsu Photonics K.K. [11], one of the three vendors that were qualified by CMS for planar pixel sensors. The details of the sensor design and production are described in refs. [7, 12].

The sensors were bump bonded to RD53A readout chips with SnAg bumps at the Fraunhofer Institute for Reliability and Microintegration (IZM) in Berlin, Germany [13]. The RD53A chip measures 20.0 mm × 11.6 mm and is produced in 65 nm CMOS technology at Taiwan Semiconductor Manufacturing Company, Ltd. (TSMC) [14]. The 50 µm × 50 µm cells of the chip are arranged in a matrix of 400 columns and 192 rows. To interconnect a sensor with 100 µm × 25 µm pixels to the RD53A chip, a metal routing from the implants to the bump bond pads on the sensors is required.

To be able to evaluate various readout schemes at a reduced production cost, the RD53A chip contains three different analog front-end circuits that are designed to meet the HL-LHC requirements in terms of radiation hardness, high hit rate, and stable operation at low thresholds. The first 128 columns of the ROC are equipped with the *Synchronous front-end*, the next 136 columns with the *Linear front-end* [15], and the last 136 columns with the *Differential front-end*. All the studies presented in this paper are performed using the *Linear front-end* (LIN FE), as this has been chosen for the final CMS IT readout chip [9].

The IT sensor R&D program is focused on the evaluation of prototype pixel sensor assemblies with the RD53A chip, with an emphasis on their performance for radiation fluences reached at the end of the HL-LHC running phase. Pixel modules of various sensor designs have been irradiated to fluences in the range $\Phi_{eq} = 4.4 \times 10^{15}\,\mathrm{cm}^{-2}$ to $2.1 \times 10^{16}\,\mathrm{cm}^{-2}$ using 25 MeV protons at the ZAG Zyklotron AG in Karlsruhe, Germany [16] or using 27 MeV protons at the MC40 cyclotron facility at the University of Birmingham [17]. The readout chip was not powered during irradiation. The sensors have not been subjected to any additional annealing other than during short periods of handling and transport at room temperature. A list of the modules studied in this paper is presented in table 2.

The particle energies correspond to the kinetic energies at extraction from the cyclotrons and a drop of approximately 2 MeV is expected during the beam delivery to the devices. While the

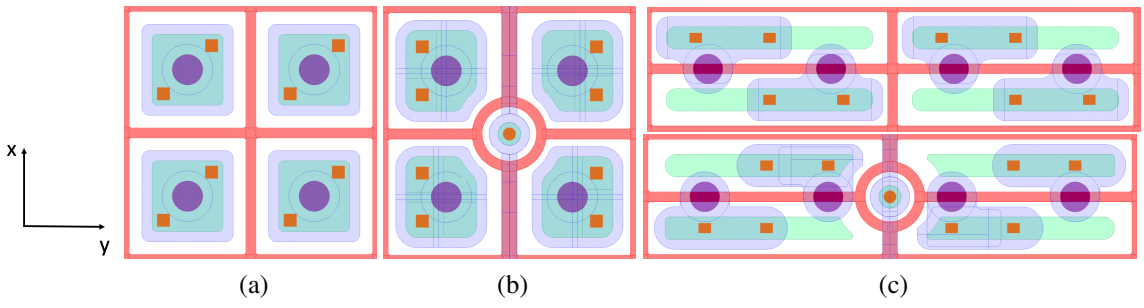

Figure 2. The layout of a 50 µm × 50 µm pitch sensor (a) without and (b) with a bias dot. The corresponding layouts for 100 µm × 25 µm pitch sensors are shown in (c). The color code indicates the various mask layers: n^+ implant (green), p-stop implant (red), metal contact via (filled orange squares), metallization (blue), and opening in the passivation for bump bonding (purple).

2023 JINST 18 P11015

Table 2. Pixel modules studied in this paper. Modules M563i and M564i were irradiated at the MC40 cyclotron facility in Birmingham while the others were irradiated at the ZAG Zyklotron AG in Karlsruhe. The numbers in the last column refer to relevant figure numbers in this paper.

ID	Pitch (μm^2)	Bias dot	Φ_{eq} (cm^{-2})	Threshold (e)	Figure
Crosstalk measurements					
M529	100×25	Yes	0	900	6
Efficiency measurements					
M547	50×50	No	4.4×10^{15}	1200	8
M564i	50×50	No	5.4×10^{15}	1200	8
M542	100×25	No	7.4×10^{15}	1320	8
M563i	100×25	No	1.0×10^{16}	1200	8
M589	100×25	No	2.1×10^{16}	1240	8
Bias dot measurements					
M521	50×50	Yes	5.3×10^{15}	1230	9
Resolution measurements					
M563	100×25	No	0	700	10
M564	50×50	No	0	600	10
M521	50×50	Yes	5.3×10^{15}	1230	10

average energy of charged particle primaries in CMS is much larger than 23 MeV, NIEL scaling [18] makes it possible to compare the effects of bulk radiation damage at different particle energies. The NIEL scaling hypothesis assumes that the concentration of irradiation induced bulk defects depends only on the NIEL. The measured 1 MeV neutron equivalent hardness factor for 23 MeV protons is 2.2 ± 0.4 [19]. Irradiations of CMS pixel prototype modules with higher energy protons, resulting in a much reduced TID in the readout chip, are under way for comparison.

3 Tuning and operation of RD53A modules

The BDAQ53 data acquisition system was used to configure, tune, and operate the RD53A modules [20]. A Xilinx KC705 evaluation board [21] was employed as the hardware platform for the system. The software part of the BDAQ53 is developed in the Python programming language and provides a set of scripts for tuning and measurement purposes.

The RD53A ROC is designed for serial powering, which is the chosen powering scheme for the CMS IT Phase-2 Upgrade [22]. However, the RD53A chip also offers the possibility of bypassing the internal power regulator to directly supply power from external units. The latter powering scheme was used in the measurements presented in this paper.

A schematic diagram of the LIN FE is shown in figure 3. The readout chain begins with a low-power charge sensitive amplifier (CSA) featuring a Krummenacher feedback circuit in order to cope with the increased leakage current of the sensor after irradiation. The output of the CSA is digitized using a high-speed current comparator and transimpedance amplifier, and is then processed by the digital pixel logic including a 4-bit Time-over-Threshold (ToT) counter (not shown in the

2023 JINST 18 P11015

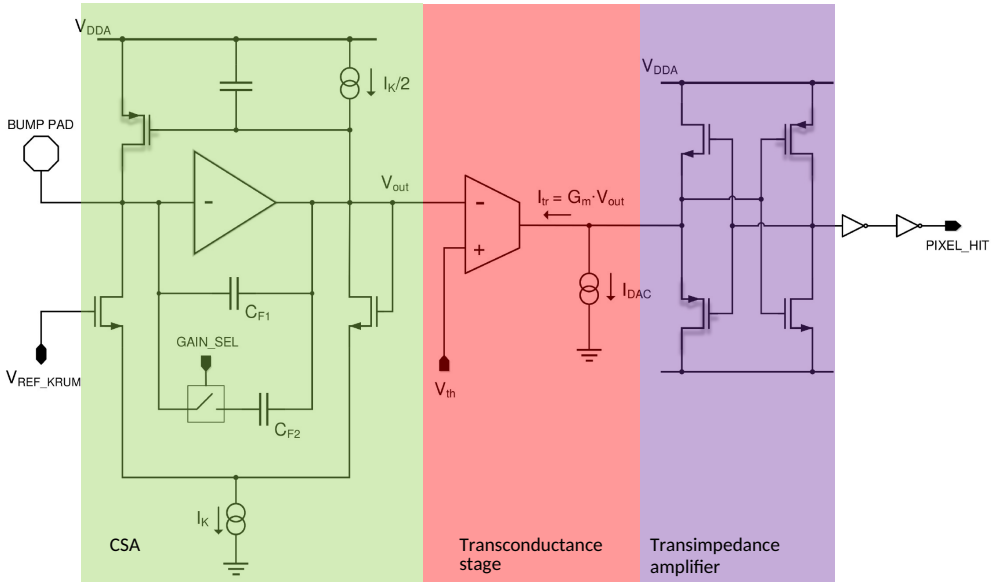

Figure 3. Schematic diagram of the RD53A *Linear front-end* [8].

figure). The global threshold for all pixels is applied to the V_{th} input of the comparator. A 4-bit binary weighted digital-to-analog converter (DAC) allows for per-pixel threshold adjustment (trimming DAC, TDAC). All pixels of the RD53A chip are equipped with an individual charge injection circuit for test and calibration purposes.

The LIN FE is configured using a number of DAC settings. A short summary of the meaning of the main DAC registers, taken from ref. [15], is given here:

- Vthreshold_LIN sets the global threshold of the *Linear front-end*, corresponding to the DC threshold voltage V_{th} applied to the discriminator input. Increasing Vthreshold_LIN results in an increased global threshold.
- LDAC_LIN sets the output dynamic range of the in-pixel threshold trimming DAC (TDAC) that determines the current I_{DAC}. Increasing LDAC_LIN results in an increased output range of the threshold adjustment.
- KRUM_CURR_LIN sets the current in the Krummenacher feedback I_{K}, used to discharge the preamplifier feedback capacitance with a constant current. Increasing KRUM_CURR_LIN results in a faster preamplifier return to baseline and a reduced ToT.
- FC_BIAS_LIN sets the current in the preamplifier folded cascode branch.
- COMP_LIN sets the bias current in the threshold discriminator input stage.
- PA_IN_BIAS_LIN sets the current in the preamplifier input branch. This current represents the main contribution to the *Linear front-end* current consumption. A decrease of PA_IN_BIAS_LIN reduces the chip power, at the cost of increased noise.
- REF_KRUM_LIN sets the preamplifier output DC baseline.

2023 JINST 18 P11015

The values of the DAC parameters used for the operation of the modules are listed in table 3. The initial values for the DACs are based on recommendations from the front-end designers. In addition to the global threshold mentioned above, the current in the Krummenacher feedback (I_{k}) and the current in the comparator (I_{DAC}) are the other primary settings of the LIN FE.

The current in the Krummenacher feedback system affects the duration of the signal discharge. Its default DAC value, KRUM_CURR_LIN = 29, is chosen so that a signal of 6000 e results in an average of 6 ToT units, where one ToT unit corresponds to 25 ns. For comparison, the most probable value for the signal generated in a non-irradiated 150 µm thick silicon sensor similar to the ones investigated in this paper was measured to be around 11 000 e, while 90% of the events have a signal below 19 000 e. To study sensor performance, KRUM_CURR_LIN is reduced to 20 for measurements of the spatial resolution in order to increase the discharge time. This forces large signals originating from single-pixel clusters to concentrate in the last few ToT bins and provides more bins for smaller signals in multi-pixel clusters, hence improving the accuracy in the measurement of the charge sharing and ultimately the performance of the algorithm used to determine the hit position of a particle. It should be noted that longer ToT results in longer pixel deadtime which is a critical parameter at high hit rates. Therefore, for the operation of the inner IT layers a compromise between charge resolution and deadtime has to be found.

For all measurements at room temperature, the default value of LDAC_LIN = 130 was used. For measurements of irradiated modules at temperatures below 0 °C, this value was increased to 185. This increases the output range of the per-pixel threshold adjustment and mitigates saturation of the trimming DAC owing to larger threshold dispersion. For the module irradiated to a fluence of $\Phi_{\mathrm{eq}} = 2.1 \times 10^{16}\,\mathrm{cm}^{-2}$, LDAC_LIN = 200 was used.

The global threshold, Vthreshold_LIN, is set for each module individually to achieve the lowest possible threshold while keeping the Equivalent Noise Charge (ENC) below 100 e and the number of noisy pixels below one percent after per-pixel adjustment. A pixel is considered noisy if it has a noise hit probability $> 2 \times 10^{-5}$ in a 25 ns sensitive time window, which corresponds to 2 hits in 1×10^{5} random triggers. Per-pixel threshold adjustment is performed in two steps, using the charge injection system. First, the threshold of each pixel is adjusted using a series of iterative threshold scans at a high global threshold of approximately 2500 e. In each iteration, the threshold of each pixel is compared to the mean of the thresholds of all pixels and its TDAC is adjusted in order to minimize the width of the threshold distribution. This results in a set of TDAC values for all pixels. Next, the ROC is configured using the TDAC values obtained in the first step and the trimming procedure is performed again at a lower global threshold of around 1000 e. This step produces a set of fine-tuned TDAC values for low-threshold operation. The other parameters remained the same for all reported measurements except for the module irradiated to the highest fluence, where a different set of parameters was necessary as mentioned above (table 3).

The tuning results for a non-irradiated module with 50 µm × 50 µm pixel size at room temperature and with a sensor bias voltage of 120 V are shown in figure 4. As visible in figure 4a, the distribution of the TDAC values after the tuning procedure for all pixels has an apparent double-peak structure, while a Gaussian distribution is expected. This feature is not present anymore in the next version of the chip. The distribution has a mean of 7.9 and a standard deviation of 3.0. The threshold is determined using the charge injection system of the RD53A chip. A voltage step supplied to the charge injection capacitors determines the quantity of the injected charge. The amplitude of

2023 JINST 18 P11015

Table 3. The DAC settings for the LIN FE used in the measurements of non-irradiated and irradiated modules. Different values of Vthreshold_LIN were used for different modules, hence the ranges of DAC values are listed. The 1 MeV neutron equivalent fluences Φ_{eq} are in cm^{-2} and total ionizing dose (TID) is in MGy. As explained in the text, in the measurements of the spatial resolution KRUM_CURR_LIN = 20 was used, while 29 was used in other measurements.

DAC name	$\Phi_{eq} = 0$ TID = 0	$0 < \Phi_{eq} \leq 1.0 \times 10^{16}$ $0 < \text{TID} \leq 13$	$\Phi_{eq} = 2.1 \times 10^{16}$ TID ≈ 30
Vthreshold_LIN	340 to 360	340 to 360	354
LDAC_LIN	130	185	200
KRUMM_CURR_LIN	29 or 20	29 or 20	20
FC_BIAS_LIN	20	20	20
COMP_LIN	110	110	110
PA_IN_BIAS_LIN	350	350	250
REF_KRUM_LIN	300	300	300

the voltage step, ΔVCAL, is controlled by the difference of two 12-bit voltage DAC outputs. The corresponding difference in DAC units between the two DACs is referred to as ΔCAL. Following the recommendation of the RD53A designers, the following conversion equation between ΔCAL and the charge Q in units of the elementary charge e is used:

$$Q(\text{e}) = \Delta\text{CAL} \cdot 10.02\,(\text{e}) + 64\,(\text{e}). \tag{3.1}$$

The ΔCAL is scanned over a range of voltages and for each voltage the corresponding charge is injected into each pixel 100 times. The injections are performed according to a pattern so that charges are not injected into neighboring pixels at the same time. The pattern is then shifted to cover all pixels. After each pattern injection all of the pixels are read out. The pixel occupancy is defined as the total number of pixels above threshold (hits) divided by the total number of injections as:

$$\text{Occupancy} = \frac{N_{\text{hit}}}{N_{\text{injection}}}. \tag{3.2}$$

Plotting the occupancy for an individual pixel as a function of the amplitude of the injected charge (ΔCAL) results in an S-curve, which is fitted with an error function. The value of ΔCAL at 50% occupancy determines the threshold of an individual pixel. Figure 4b shows the overlay of S-curves for all *Linear front-end* pixels in a single ROC, where the number of pixels in a particular bin is indicated by the color-scale. The distribution of the pixel thresholds is shown in figure 4c. The mean threshold for this module is 640 e with a variation between the pixels given by a standard deviation of 75 e. A fit is reported as failed if the ΔVCAL-range selected for the threshold scan is too small, if $\chi^2/\text{DOF} > 40$, or if the occupancy does not increase with ΔVCAL for a given pixel. The number of failed fits for this module is negligible. The sigma of the error function is taken to be the ENC. The module has a mean ENC of 83 e with a standard deviation of 7 e, as shown in figure 4d.

Figure 5 illustrates a similar set of plots for a module irradiated with protons at the MC40 cyclotron facility in Birmingham to a fluence of $\Phi_{eq} = 5.4 \times 10^{15}\,cm^{-2}$. This corresponds to a total ionizing dose of 7.7 MGy in silicon dioxide, relevant for surface damage in the sensor. The

2023 JINST 18 P11015

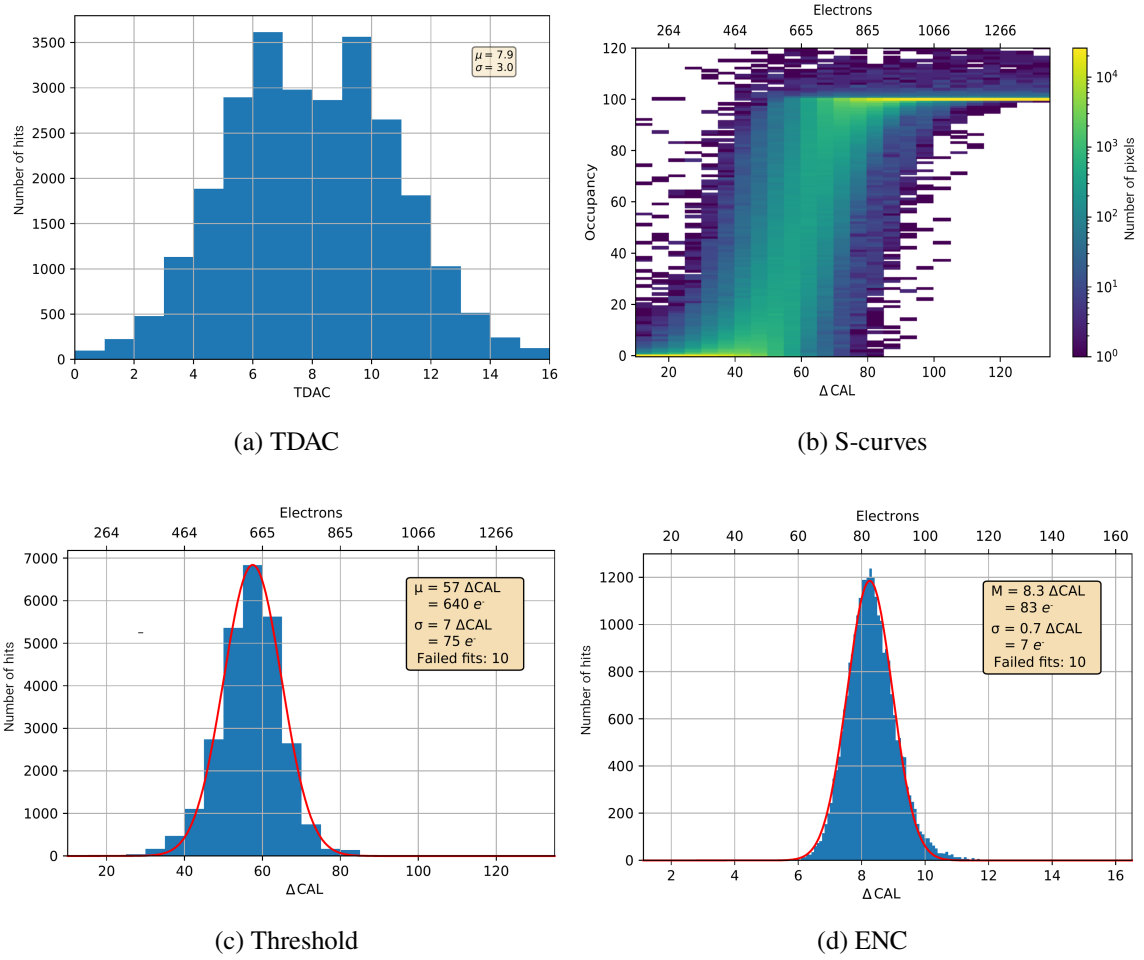

(a) TDAC

(b) S-curves

(c) Threshold

(d) ENC

Figure 4. (a) Distribution of TDAC, (b) S-curves for all pixels, (c) distribution of trimmed thresholds with Gaussian fit, and (d) ENC distribution with Gaussian fit after tuning the ROC for a non-irradiated module with 50 µm × 50 µm pixel size at room temperature and with a sensor bias voltage of 120 V.

tuning was performed for a sensor temperature of approximately −30 °C with a sensor bias voltage of 200 V. A significant number of pixels have TDAC values of 0 or 15, a sign that the dynamic range of the TDAC circuit is not sufficient to compensate for the threshold dispersion after irradiation. The mean threshold has increased significantly to 1230 e, and the threshold and ENC distributions have larger spreads after irradiation: 144 e and 11 e, respectively. The number of failed fits has increased to 97, which is in the range of 0.4% of all pixels in the *Linear front-end*.

4 Crosstalk

To be able to bump bond a sensor with a pixel pitch of 100 µm × 25 µm to the RD53A chip, which has a bump bond pattern of 50 µm × 50 µm, the bump bonding pads on the sensor are placed on the boundary between two neighboring pixels, as shown in figure 2c. These pads overlap with the implant layer of the neighboring pixels, and as a result crosstalk between the two pixels via

2023 JINST 18 P11015

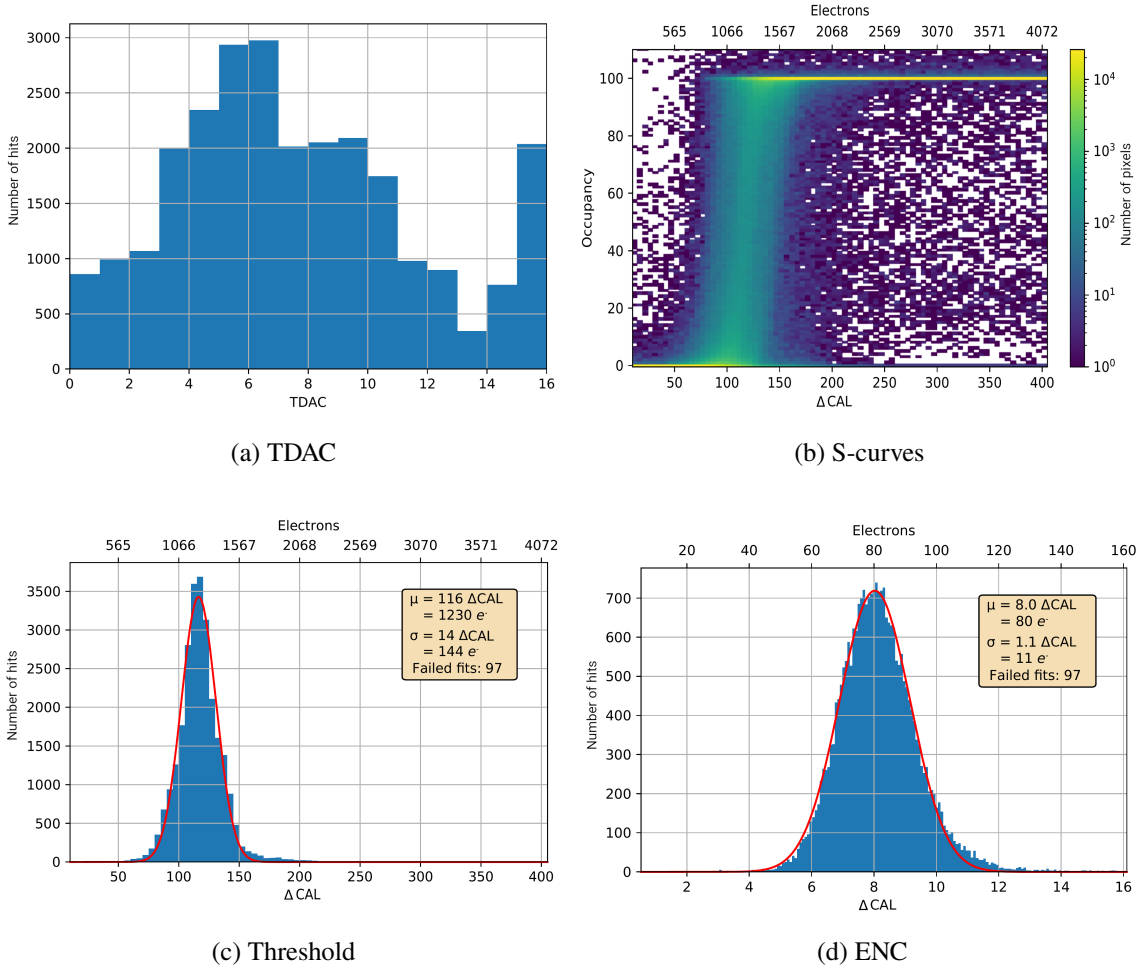

(a) TDAC

(b) S-curves

(c) Threshold

(d) ENC

Figure 5. (a) Distribution of TDAC, (b) S-curves for all pixels, (c) distribution of trimmed thresholds with Gaussian fit, and (d) ENC distribution with Gaussian fit after tuning the ROC for a module with 50 µm × 50 µm pixel size irradiated to a fluence of $\Phi_{eq} = 5.3 \times 10^{15}$ cm^{-2}. The tuning was performed at approximately −30 °C with a sensor bias voltage of 200 V. The TDAC distribution shows a significant number of entries in the last bin because of the saturation of the dynamic range of the TDAC circuit at low temperatures. In the next generation of the chip, this issue has been addressed by adding an additional bit to the TDAC circuit. The entries with low occupancy at high injection voltages in the S-curve plot are likely associated with the combination of this feature and the accumulated irradiation damage.

capacitive coupling is observed. The amount of crosstalk is determined from S-curve scans using the charge injection system of the RD53A chip as described in section 3. In the absence of crosstalk, the maximum pixel occupancy should remain at 100% regardless of the injection amplitude. In case of crosstalk, a charge injected into a single pixel leads to a charge above threshold also in the neighbor pixel, provided that the injected charge is large enough. The plot of occupancy versus ΔCAL therefore shows a second S-curve leading to an occupancy of up to 200%. The point where the mean occupancy is 150%, ΔCAL_{150}, is the amount of charge injected in units of ΔCAL that leads to half of the injections resulting in the signal of a neighbor pixel going above threshold. As seen in figure 6a

2023 JINST 18 P11015

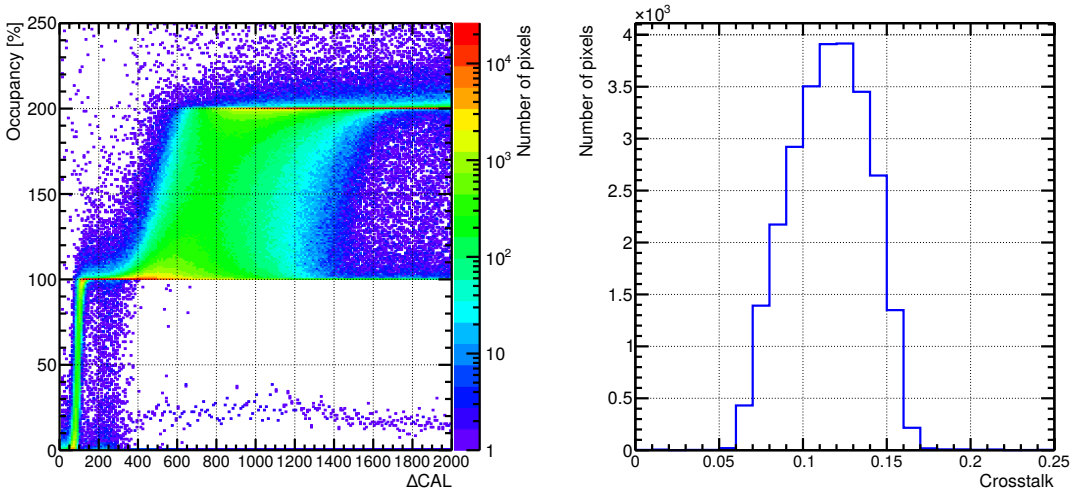

(a) (b)

Figure 6. (a) Occupancy versus ΔCAL for a non-irradiated RD53A module with a sensor with pixel cell size of 100 µm × 25 µm. Crosstalk leads to a double S-curve. (b) The crosstalk distribution for all pixels. An average crosstalk of approximately 11% is observed in these modules. The measurements were performed at room temperature and a bias voltage of 120 V.

for a sensor with 100 µm × 25 µm pixel size, this kind of double S-curve is present. In sensors with 50 µm × 50 µm pixel size the occupancy remains at 100% even at very high injection amplitudes.

The double S-curve of each pixel is fitted using error functions to determine the ratio of the ΔCAL at 50% occupancy (ΔCAL_{50}) to the ΔCAL at 150% occupancy (ΔCAL_{150}) for each pixel:

$$\text{Crosstalk} = \frac{\Delta CAL_{50}}{\Delta CAL_{150}}. \tag{4.1}$$

The distribution of crosstalk for all pixels at a global threshold of 900 e is shown in figure 6b. The mean crosstalk is approximately 11%. TCAD simulations show that a semi-circular cutout in the implant just under the bump bonding pads reduces the capacitive coupling to the neighbor pixel from about 21 to 14 fF, thereby reducing the crosstalk. Such a design has been implemented in later production submissions [23].

5 Sensor evaluation with particle beams

The performance of the pixel modules has been evaluated using electron beams at the DESY-II testbeam facility [24]. DESY-II is an electron/positron synchrotron that offers secondary beams with user-selectable momenta from 1 to 6 GeV/c. The data for the studies presented in this paper were taken with electron beams of 3 GeV/c.

The testbeam facility is equipped with EUDET-type pixel beam telescopes [25] for particle tracking. The DATURA beam telescope at beam line 21 and the AZALEA beam telescope at beam line 24 were used in the following studies. A schematic side view of the setup at the beam line

2023 JINST 18 P11015

is shown in figure 7a. Each telescope consists of six planes, divided into an upstream arm and a downstream arm, with three planes each. The device under test (DUT) was mounted on a movable stage between the two arms. The integration time of the 50 µm thick MIMOSA-26 chips [26] used in the telescope is 115.2 µs, corresponding to 115 turns of the DESY-II synchrotron. Owing to such a long integration time, multiple tracks are present in each telescope event, referred to as pileup. A CMS Phase-1 pixel module (150 µm × 100 µm pixel size) [4] with an integration time of 25 ns was placed in front of the upstream arm as a timing reference to reduce pileup of telescope tracks in the analysis. The reference module was inclined around the x and y axes to improve its spatial resolution.

Non-irradiated modules were mounted on an aluminium frame and measured at the ambient temperature of the experimental hall. Irradiated modules were mounted inside a thermally insulated coldbox, which kept the modules at low temperatures in order to reduce the leakage current (figure 7b). The box was cooled down using a chiller and two Peltier elements. The chiller was set to a temperature

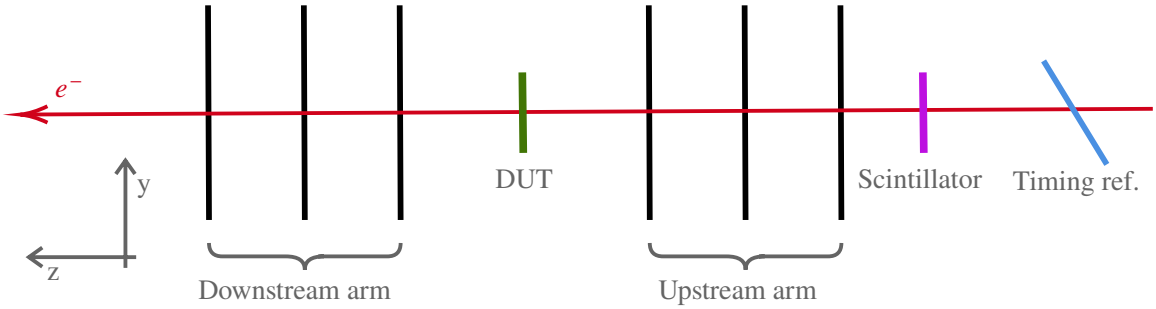

(a)

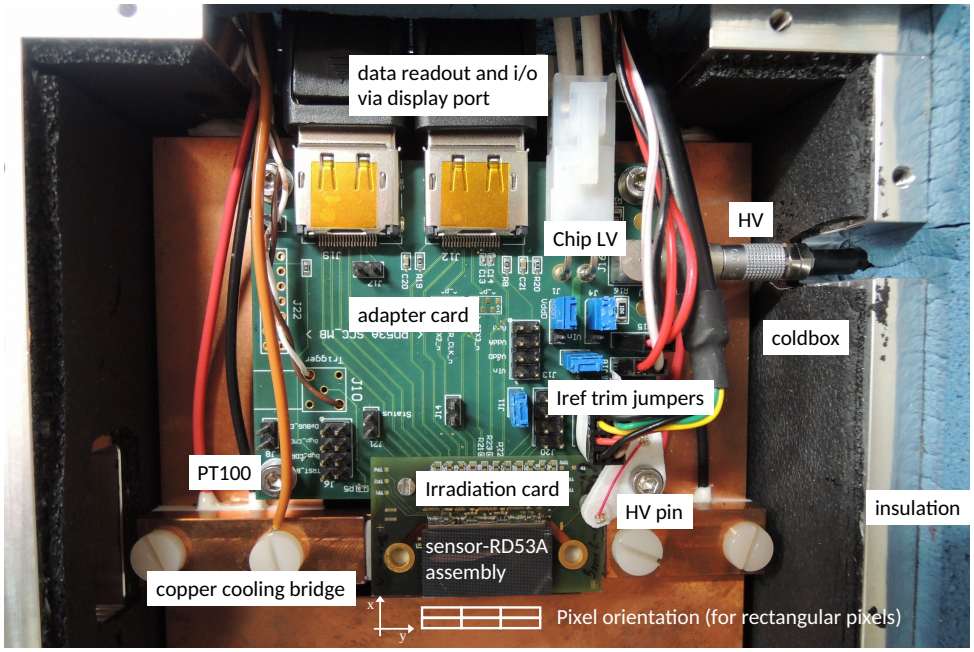

(b)

Figure 7. (a) Schematic side view of the testbeam setup with the global testbeam and telescope coordinate system. (b) A RD53A module mounted inside the coldbox.

2023 JINST 18 P11015

of −25 °C. The box was continuously flushed with dry air to prevent condensation. Under these conditions, the temperature of the sensor is estimated to be approximately −30 °C. The support for the DUT included a rotation stage with the axis of rotation pointing upward (in the telescope y direction). For sensor modules with 100 µm × 25 µm pixel size, the entire support frame or cold box was rotated by 90° with respect to the orientation shown in figure 7b when rotations around the long pixel side were desired. Independent of the orientation of the DUT, resolution plots always refer to local sensor coordinates where x is the coordinate parallel to the 25 µm pixel side. The telescope, DUT, and reference module were synchronized using a common trigger signal, which was generated by the coincidence of a pair of trigger scintillators placed upstream of the first telescope plane.

5.1 Data analysis

In the first step of the data analysis, tracks in the six telescope planes are reconstructed and used to determine the relative positioning of the planes (telescope alignment). Since the track reconstruction requires alignment and alignment requires reconstructed tracks, the process starts using loose cuts on the maximum spatial distance between clusters in the planes and a track and is refined in an iterative manner to achieve tighter cuts and improved alignment. In each iteration the position and rotation of each telescpe plane is corrected using the parameters of the reconstructed tracks.

In the next step, telescope tracks are extrapolated to and checked against the hits in the reference module to remove out-of-time tracks. Tracks within a distance of 150 µm in x and 100 µm in y from a hit in the reference module are accepted and are used to determine the relative alignment of the reference module. These tracks are also used in any subsequent analysis.

The last step involves performing the alignment of the DUT by extrapolating the tracks to the position of the DUT. Owing to the presence of a copper bar behind the DUT in the coldbox, the downstream track resolution is significantly deteriorated for data taken with irradiated modules. Therefore, only the upstream triplet is used for the alignment and analysis in this case. For modules with 100 µm × 25 µm pixel size, hits in the DUT within a distance from a track of 150 µm in the long pixel direction and 100 µm in the short pixel direction are assigned to the track. For modules with 50 µm × 50 µm pixel size, hits within a 100 µm distance in both directions are accepted. A hit is defined as a pixel with a signal above threshold. Adjacent hit pixels are combined into a cluster and its position in local coordinates is calculated as the weighted mean of the pixel positions with the pixel charges in units of ToT as weights (center-of-gravity reconstruction method). The difference between the extrapolation of the track and the position of the cluster in the DUT is used to determine the alignment of the DUT with respect to the telescope. Six alignment parameters are determined for the DUT: three local position coordinates and three rotation angles.

5.2 Hit efficiency

The hit efficiency is studied for non-irradiated and irradiated pixel modules. It is defined as:

$$\epsilon_{\text{hit}} = \frac{N_{\text{hit}}}{N_{\text{t}}}, \tag{5.1}$$

where N_{hit} is the number of reconstructed in-time tracks with a hit on the DUT within an acceptance region that corresponds to the *Linear front-end*, excluding its two last rows and columns, and N_{t} is the total number of tracks traversing the DUT.

2023 JINST 18 P11015

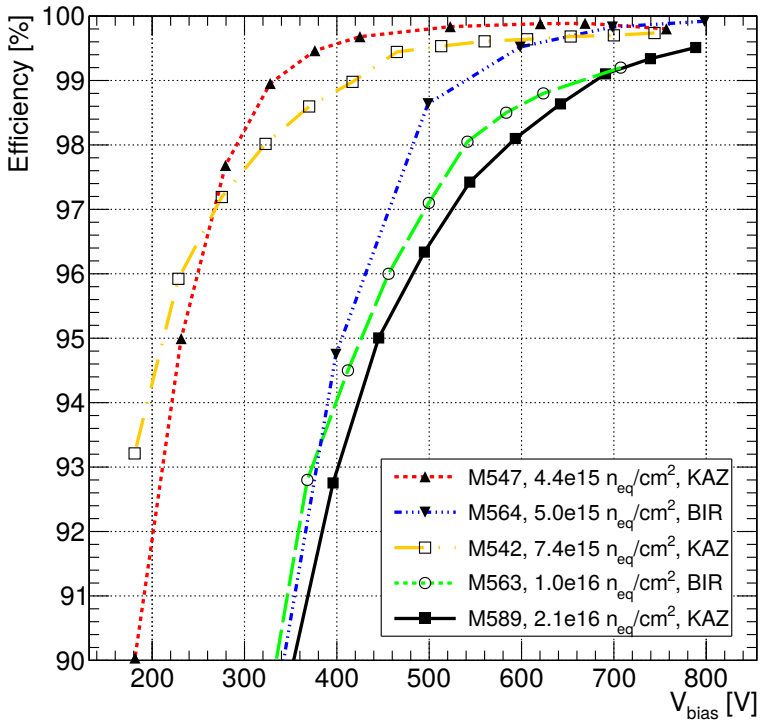

Figure 8. Efficiency as a function of bias voltage for RD53A sensor modules without a bias dot after irradiation with protons at the Karlsruhe Cyclotron (KAZ) and at the MC40 cyclotron facility in Birmingham (BIR). All modules have been measured at a temperature below −25 °C at vertical incidence and achieve an efficiency in excess of 99%.

Non-irradiated modules without a bias dot achieve an efficiency greater than 99% at bias voltages as low as 10 V, which is well below the full depletion voltage of ≈ 75 V.

Modules without a bias dot irradiated to fluences of $\Phi_{eq} = 4.4, 5.4, 7.4, 10$, and 21×10^{15} cm^{-2} were investigated. As shown in figure 8, all these modules reach 99% hit efficiency. Although significantly higher bias voltages are required to reach the efficiency goal, these voltages are still below the 800 V limit considered for the operation in CMS. It is not understood why the efficiency curve for M542 is systematically above the one for M564 despite the larger fluence.

Modules with a punch-through bias dot suffer from charge loss when a particle hits the bias dot at a small angle with respect to the module normal. Hence, a hit inefficiency in the vicinity of the bias dot is expected, as shown in figure 9a, which displays the efficiency as a function of impact position in a 2 pixel × 2 pixel cell at a bias voltage of 250 V. A voltage well below full depletion was chosen for this study to enhance the effect. This is a module with 50 µm × 50 µm pixel size irradiated to a fluence of $\Phi_{eq} = 5.3 \times 10^{15}$ cm^{-2}. The pointing resolution of the beam telescope at the DUT is on the order of 8 µm for this measurement. The efficiency as a function of bias voltage for different angles of incidence is shown in figure 9b. An efficiency in excess of 99% is achieved for bias voltages above 350 V for incident angles above 20°. Based on the studies presented in this section, CMS has chosen sensors without punch-through bias dots for the upgrade of the IT.

2023 JINST 18 P11015

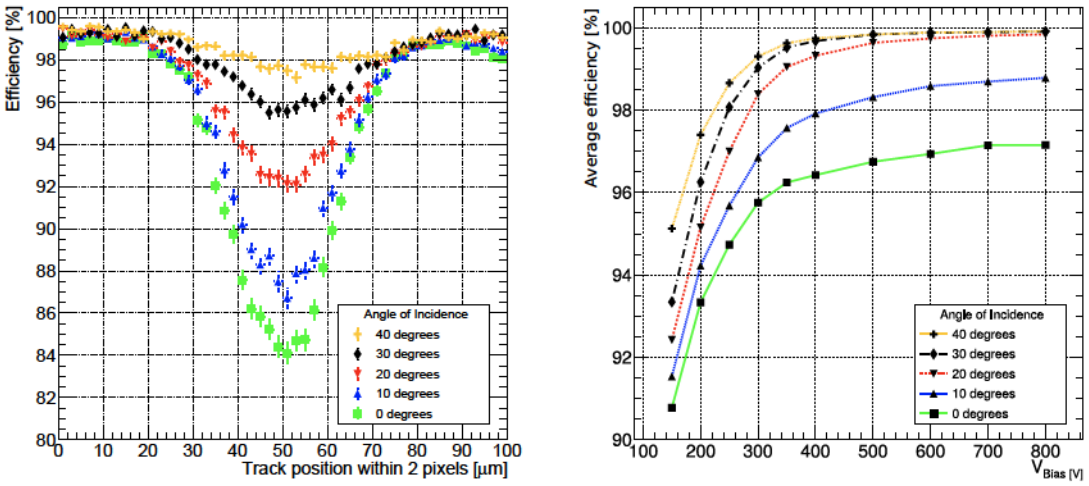

(a) (b)

Figure 9. (a) Efficiency as function of position in a 2 pixel × 2 pixel cell for a 50 µm × 50 µm pitch sensor with a punch-through bias dot irradiated to $\Phi_{eq} = 5.3 \times 10^{15}$ cm^{-2} for different incident angles and measured at a bias voltage of 250 V. (b) Efficiency as a function of bias voltage for the same module for a variety of incident angles. Irradiated modules are measured at a temperature below −25 °C. These data are also published in ref. [12].

5.3 Spatial resolution

To determine the spatial resolution of a pixel module, first the distance in the local x coordinate of a cluster in the DUT (x_{DUT}) to the impact point of the telescope track extrapolated to the DUT (x_{track}) is calculated for each event as:

$$\Delta x = x_{\text{DUT}} - x_{\text{track}}. \tag{5.2}$$

Then the resulting residual distribution is fitted using a generalized Gaussian distribution [27] in a range of three standard deviations from the peak of the distribution:

$$g_{\text{gen}}(\Delta y) = B_g + \frac{A_g \cdot S_g}{\sqrt{8} \cdot \sigma_g \cdot \Gamma(1/S_g)} \cdot \exp\left(- \left| \frac{\Delta y - \mu_g}{\sqrt{2} \cdot \sigma_g} \right|^{S_g} \right) \tag{5.3}$$

where Γ is the Gamma function and all variables with a g subscript are fit parameters.

More recent studies have used the RMS of the residual distribution restricted to a certain range instead of a fit to evaluate the spatial resolution. This method is preferred for angles close to vertical incidence where the distributions are box-like and not Gaussian. However, using the RMS requires additional cuts not used in this analysis to reject outliers, which would strongly bias the RMS. The spatial resolution of the pixel module in x direction is obtained from the standard deviation of the fitted generalized error function by subtracting the telescope resolution in quadrature.

The spatial resolution as a function of the angle of incidence for 50 µm × 50 µm pitch sensors before and after irradiation and for a non-irradiated 100 µm × 25 µm pitch sensor is shown in figure 10, while selected residual distributions fitted with generalized error functions are shown

2023 JINST 18 P11015

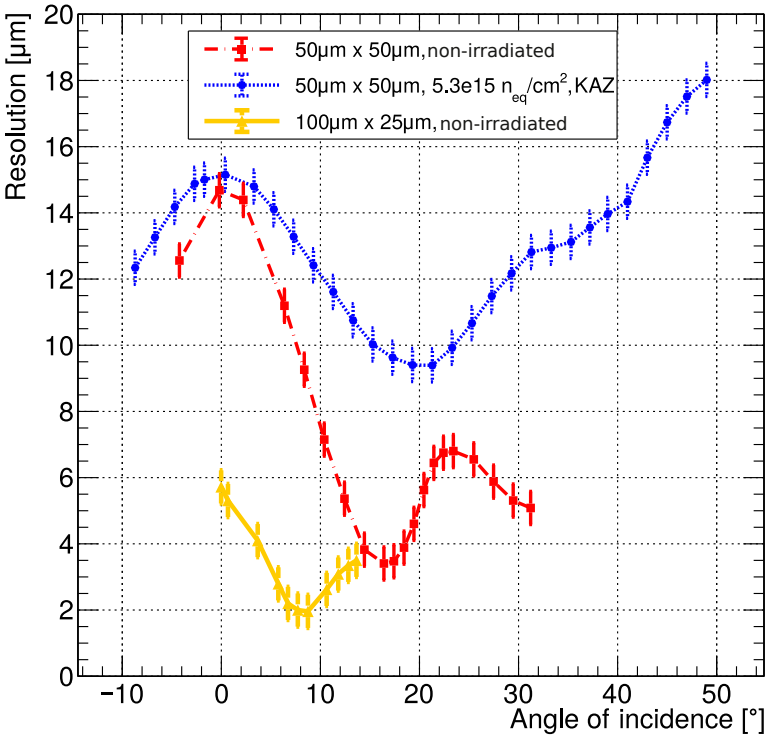

Figure 10. Spatial resolution as a function of incidence angle for RD53A modules equipped with a 50 µm × 50 µm or 100 µm × 25 µm sensor. The modules are rotated around an axis that is parallel to the 100 µm pixel side for sensors with rectangular pixels, and the resolution is determined in the coordinate parallel to the 25 µm side. The non-irradiated modules were measured at room temperature at a bias voltage of 120 V. The irradiated module was measured at a temperature below −25 °C and a bias voltage of 800 V. The optimum angle for charge sharing is clearly visible for non-irradiated and irradiated sensors.

in figure 11. The non-irradiated modules were measured at room temperature at a bias voltage of 120 V. The irradiated module was measured at a temperature below −25 °C and a bias voltage of 800 V. The results shown in figure 10 are after subtraction of the telescope resolution in quadrature. The telescope resolution depends on the beam momentum, the spacing of the telescope planes, and the distance between the DUT and the neighboring telescope planes. In case of the non-irradiated modules, the telescope resolution is estimated using upstream and downstream triplet tracks, extrapolated to the DUT plane. It is 4.3 ± 0.5 µm and 3.8 ± 0.5 µm for the setup with the module with 50 µm × 50 µm and 100 µm × 25 µm pixel size, respectively. This small difference is simply a result of two independent measurements with slightly different positions of the DUT with respect to the closest telescope planes. For the irradiated module a telescope resolution of 7.6 µm is subtracted, using only the three upstream telescope planes. In this case, the telescope resolution is obtained by placing a non-irradiated module with known resolution in the cold box with the same telescope configuration and measuring the residual distribution. A systematic uncertainty of 0.5 µm on the final results is estimated.

2023 JINST 18 P11015

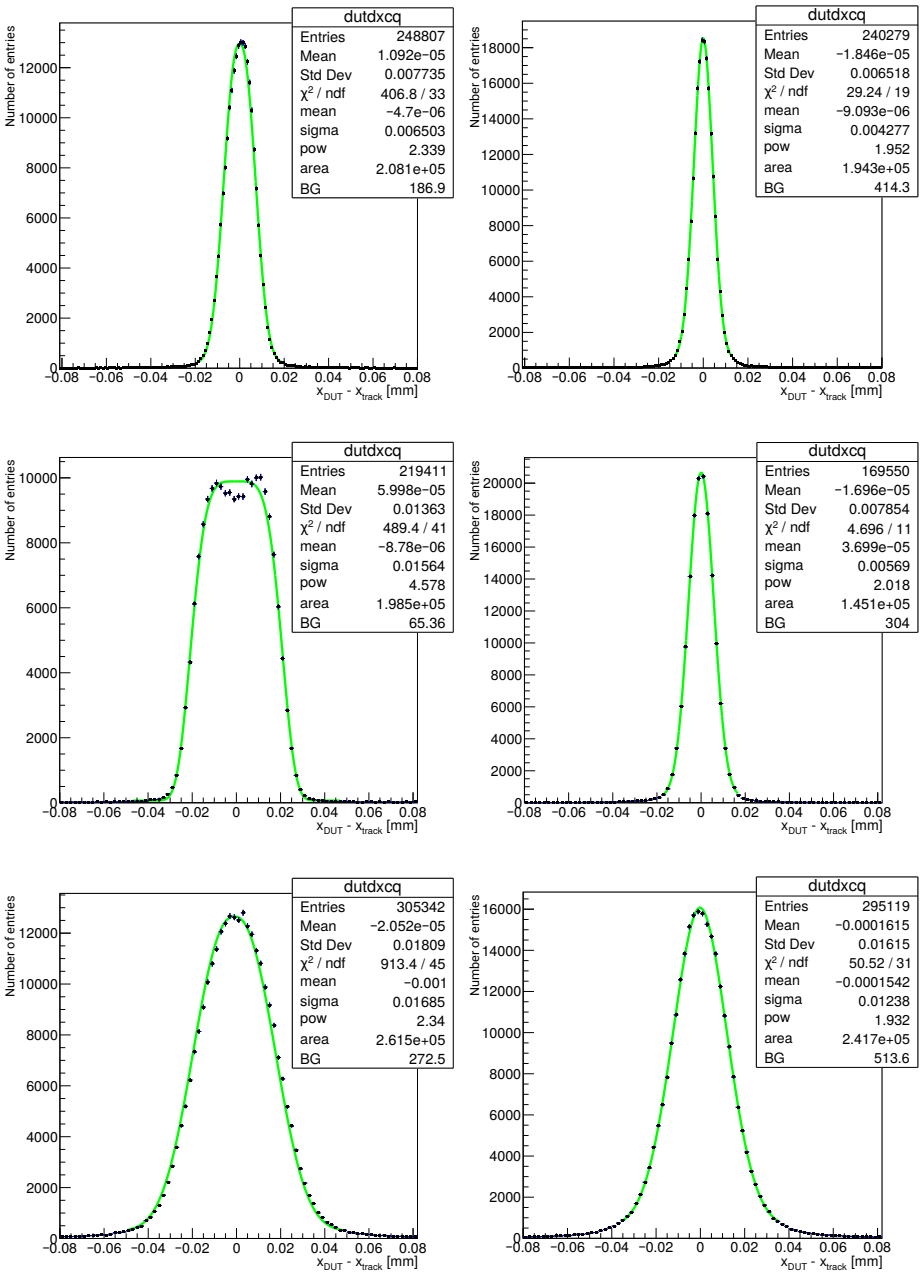

Figure 11. Residual distributions fitted with generalized error functions at vertical incidence (left) and at the optimal angle (right) for modules M563 (100 µm × 25 µm sensor, non-irradiated) (top), M564 (50 µm × 50 µm sensor, non-irradiated) (center), and M521 (50 µm × 50 µm sensor, $\Phi_{\mathrm{eq}} = 5.3 \times 10^{15}$ cm^{-2}) (bottom). The fit parameters listed under χ^2/ndf correspong to the parameres μ_g, σ_g, S_g, A_g and B_g in equation (5.3), respectively.

For the sensor modules with 50 µm × 50 µm pixel size, a minimum hit resolution of 3.4 µm (9.4 µm) is obtained at the optimal angle of incidence,

$$\alpha_{\mathrm{opt}} = \arctan\left(\frac{\mathrm{pitch}}{\mathrm{thickness}}\right), \tag{5.4}$$

2023 JINST 18 P11015

before (after) irradiation. The optimal angle is the angle at which a track traverses exactly two pixels, which leads to the best resolution because of charge sharing. The optimal angle before irradiation is approximately 18° and increases to about 20° after irradiation, indicating a reduction in the charge collection depth. At vertical incidence, the resolution is about 14 µm in both cases, which is in agreement with the expected resolution of pitch/$\sqrt{12}$ in the absence of charge sharing within the uncertainties. For the non-irradiated sensor with 100 µm × 25 µm pixel size, a minimum spatial resolution in the 25 µm direction of 2 µm is obtained at the optimal angle of 8.5°.

6 Summary and outlook

Silicon pixel modules with planar sensors from Hamamatsu Photonics K.K. and RD53A readout chips have been built and evaluated with a particle beam. After threshold tuning, a minimum threshold of 700 e for non-irradiated RD53A-sensor assemblies and approximately 1200 e after irradiation to a fluence of up to $\Phi_{eq} = 2.1 \times 10^{16}\,cm^{-2}$ is obtained. This fluence corresponds to the highest lifetime fluence for planar sensors in the IT, which would be reached in parts of ring 1 of the forward discs, assuming ring 1 is not replaced during the HL-LHC. The current sensor design results in a crosstalk of approximately 11% in the 100 µm × 25 µm pitch modules. Based on this result and on TCAD studies, a modification of the design has been implemented in the next submission, which reduces the crosstalk by 30%. A spatial resolution of 2 µm is obtained for a non-irradiated 100 µm × 25 µm pitch sensor at the optimal angle of incidence. For a sensor module with 50 µm × 50 µm pixel size, a spatial resolution of 3.4 µm before irradiation and 9.4 µm at a fluence of $\Phi_{eq} = 5.3 \times 10^{15}\,cm^{-2}$ is reached. An efficiency in excess of 99% is achieved for modules irradiated to fluences up to $\Phi_{eq} = 2.1 \times 10^{16}\,cm^{-2}$. Assuming NIEL scaling and sufficient cooling performance, these results show that planar silicon sensor modules would survive the entire 10 year HL-LHC running program corresponding to an integrated luminosity of 4000 fb^{-1}. No replacements are needed except for barrel layer 1, where 3D sensors will be used and for which at least one replacement is foreseen. A replacement of ring 1 of TFPX might be necessary if the cooling performance becomes critical or if too many readout channels become noisy.

The sensors without the punch-through bias dot evaluated in this paper fulfill the requirements for the CMS Inner Tracker upgrade in terms of hit efficiency. Guided by tracking and physics simulation of the entire tracking system, CMS has decided to use 100 µm × 25 µm pitch sensors throughout the entire IT.

Recently, irradiations of CMS pixel prototype modules have been performed with 23 GeV protons at the CERN Proton Synchrotron, resulting in a much reduced TID in the readout chip. Single chip assemblies with the final prototype of the CMS readout chip, CROCv1, have been tested before and after irradiation. The validation of full prototype modules consisting of flexible printed circuit boards and pixel sensors interconnected to two and four RD53A and CROCv1 readout chips, respectively, is under way. These sensors feature larger pixels in the regions between readout chips to avoid dead regions. The prototyping program with CROCv1 single chip assemblies and full modules will be reported in future publications while CMS is preparing for the production of sensors, readout chips and modules for the CMS IT for Phase-2.

2023 JINST 18 P11015

Acknowledgments

The measurements leading to these results have been performed at the Test Beam Facility at DESY Hamburg (Germany), a member of the Helmholtz Association (HGF). We also thank the teams at the irradiation facilities (the Karlsruhe Compact Cyclotron (KAZ) and Birmingham MC40) for their support.

The tracker groups gratefully acknowledge financial support from the following funding agencies: BMWFW and FWF (Austria); FNRS and FWO (Belgium); CERN; MSE and CSF (Croatia); Academy of Finland, MEC, and HIP (Finland); CEA and CNRS/IN2P3 (France); BMBF, DFG, and HGF (Germany); GSRT (Greece); NKFIA K124850, and Bolyai Fellowship of the Hungarian Academy of Sciences (Hungary); DAE and DST (India); INFN (Italy); PAEC (Pakistan); SEIDI, CPAN, PCTI and FEDER (Spain); Swiss Funding Agencies (Switzerland); MST (Taipei); STFC (United Kingdom); DOE and NSF (U.S.A.). This project has received funding from the European Union's Horizon 2020 research and innovation program under the Marie Skłodowska-Curie grant agreement No 884104 (PSI-FELLOW-III-3i) and project AIDA-2020, GA no. 654168. Individuals have received support from HFRI (Greece).

References

[1] G. Apollinari et al., eds., *High-Luminosity Large Hadron Collider (HL-LHC): Technical Design Report V. 0.1*, Tech. Rep. CERN-2017-007-M CERN, Geneva (2017) [DOI:10.23731/CYRM-2017-004].

[2] High Luminosity LHC Project, https://hilumilhc.web.cern.ch/.

[3] CMS collaboration, *The CMS Experiment at the CERN LHC*, 2008 *JINST* **3** S08004.

[4] Tracker Group of the CMS collaboration, *The CMS Phase-1 Pixel Detector Upgrade*, 2021 *JINST* **16** P02027 [arXiv:2012.14304].

[5] CMS collaboration, *The Phase-2 Upgrade of the CMS Tracker*, Tech. Rep. CERN-LHCC-2017-009 CERN, Geneva (2017) [DOI:10.17181/CERN.QZ28.FLHW].

[6] J. Duarte-Campderros et al., *Results on proton-irradiated 3D pixel sensors interconnected to RD53A readout ASIC*, *Nucl. Instrum. Meth. A* **944** (2019) 162625 [arXiv:1903.12531].

[7] J. Schwandt, *CMS Pixel detector development for the HL-LHC*, *Nucl. Instrum. Meth. A* **924** (2019) 59.

[8] M. Garcia-Sciveres, *The RD53A Integrated Circuit*, Tech. Rep. CERN-RD53-PUB-17-001, CERN, Geneva (2017).

[9] Tracker Group of the CMS collaboration, *Comparative evaluation of analogue front-end designs for the CMS Inner Tracker at the High Luminosity LHC*, 2021 *JINST* **16** P12014 [arXiv:2105.00070].

[10] Y. Allkofer et al., *Design and performance of the silicon sensors for the CMS barrel pixel detector*, *Nucl. Instrum. Meth. A* **584** (2008) 25 [physics/0702092].

[11] Hamamatsu Photonics K.K., https://www.hamamatsu.com.

[12] Tracker Group of the CMS collaboration, *Evaluation of HPK n^+-p planar pixel sensors for the CMS Phase-2 upgrade*, *Nucl. Instrum. Meth. A* **1053** (2023) 168326 [arXiv:2212.04793].

[13] Fraunhofer Institute for Reliability and Microintegration IZM, https://www.izm.fraunhofer.de/.

[14] Taiwan Semiconductor Manufacturing Company Limited (TSMC), https://www.tsmc.com.

2023 JINST 18 P11015

[15] L. Gaioni and F. Loddo, *CMS analog front-end: simulations and measurements*, Tech. Rep. CERN-RD53-PUB-20-002, CERN, Geneva (2020).

[16] ZAG Zyklotron AG, http://www.zyklotron-ag.de.

[17] D. Parker and C. Wheldon, *The Birmingham MC40 Cyclotron Facility*, *Nucl. Phys. News* **28** (2018) 15.

[18] M. Moll, *Displacement damage in silicon detectors for high energy physics*, *IEEE Trans. Nucl. Sci.* **65** (2018) 1561.

[19] P. Allport et al., *Experimental Determination of Proton Hardness Factors at Several Irradiation Facilities*, 2019 *JINST* **14** P12004 [arXiv:1908.03049].

[20] M. Daas et al., *BDAQ53, a versatile pixel detector readout and test system for the ATLAS and CMS HL-LHC upgrades*, *Nucl. Instrum. Meth. A* **986** (2021) 164721 [arXiv:2005.11225].

[21] Xilinx, https://www.xilinx.com.

[22] V. Perovic, *Serial powering in four-chip prototype RD53A modules for Phase 2 upgrade of the CMS pixel detector*, *Nucl. Instrum. Meth. A* **978** (2020) 164436.

[23] M. Hajheidari, *Characterisation of planar sensors for the inner tracker of the CMS experiment*, 2022 *JINST* **17** C09002.

[24] R. Diener et al., *The DESY II Test Beam Facility*, *Nucl. Instrum. Meth. A* **922** (2019) 265 [arXiv:1807.09328].

[25] H. Jansen et al., *Performance of the EUDET-type beam telescopes*, *EPJ Tech. Instrum.* **3** (2016) 7 [arXiv:1603.09669].

[26] C. Hu-Guo et al., *First reticule size MAPS with digital output and integrated zero suppression for the EUDET-JRA1 beam telescope*, *Nucl. Instrum. Meth. A* **623** (2010) 480.

[27] S. Nadarajah, *A generalized normal distribution*, *J. Appl. Stat.* **32** (2005) 685.

2023 JINST 18 P11015

The Tracker Group of the CMS collaboration

Institut für Hochenergiephysik, Wien, Austria

W. Adam, T. Bergauer, K. Damanakis, M. Dragicevic, R. Frühwirth[1], H. Steininger

Universiteit Antwerpen, Antwerpen, Belgium

W. Beaumont, M.R. Darwish[2], T. Janssen, H. Rejeb Sfar, P. Van Mechelen

Vrije Universiteit Brussel, Brussel, Belgium

N. Breugelmans, M. Delcourt, A. De Moor, J. D'Hondt, F. Heyen, S. Lowette, I. Makarenko, D. Muller, A.R. Sahasransu, D. Vannerom, S. Van Putte

Université Libre de Bruxelles, Bruxelles, Belgium

Y. Allard, B. Clerbaux, S. Dansana[3], G. De Lentdecker, H. Evard, L. Favart, D. Hohov, A. Khalilzadeh, K. Lee, M. Mahdavikhorrami, A. Malara, S. Paredes, N. Postiau, F. Robert, L. Thomas, M. Vanden Bemden, P. Vanlaer, Y. Yang

Université Catholique de Louvain, Louvain-la-Neuve, Belgium

A. Benecke, G. Bruno, F. Bury, C. Caputo, J. De Favereau, C. Delaere, I.S. Donertas, A. Giammanco, K. Jaffel, S. Jain, V. Lemaitre, K. Mondal, N. Szilasi, T.T. Tran, S. Wertz

Institut Ruđer Bošković, Zagreb, Croatia

V. Brigljević, B. Chitroda, D. Ferenček, S. Mishra, A. Starodumov, T. Šuša

Department of Physics, University of Helsinki, Helsinki, Finland

E. Brücken

Helsinki Institute of Physics, Helsinki, Finland

T. Lampén, L. Martikainen, E. Tuominen

Lappeenranta-Lahti University of Technology, Lappeenranta, Finland

A. Karadzhinova-Ferrer, P. Luukka, H. Petrow, T. Tuuva[†]

Université de Strasbourg, CNRS, IPHC UMR 7178, Strasbourg, France

J.-L. Agram[4], J. Andrea, D. Apparu, D. Bloch, C. Bonnin, J.-M. Brom, E. Chabert, L. Charles, C. Collard, E. Dangelser, S. Falke, U. Goerlach, L. Gross, C. Haas, M. Krauth, N. Ollivier-Henry

Université de Lyon, Université Claude Bernard Lyon 1, CNRS/IN2P3, IP2I Lyon, UMR 5822, Villeurbanne, France

G. Baulieu, A. Bonnevaux, G. Boudoul, L. Caponetto, N. Chanon, D. Contardo, T. Dupasquier, G. Galbit, M. Marchisone, L. Mirabito, B. Nodari, E. Schibler, F. Schirra, M. Vander Donckt, S. Viret

RWTH Aachen University, I. Physikalisches Institut, Aachen, Germany

V. Botta, C. Ebisch, L. Feld, W. Karpinski, K. Klein, M. Lipinski, D. Louis, D. Meuser, I. Özen, A. Pauls, G. Pierschel, N. Röwert, M. Teroerde, M. Wlochal

2023 JINST 18 P11015

RWTH Aachen University, III. Physikalisches Institut B, Aachen, Germany
C. Dziwok, G. Fluegge, O. Pooth, A. Stahl, T. Ziemons

Deutsches Elektronen-Synchrotron, Hamburg, Germany
A. Agah, S. Bhattacharya, F. Blekman[5], A. Campbell, A. Cardini, C. Cheng, S. Consuegra Rodriguez, G. Eckerlin, D. Eckstein, E. Gallo[5], M. Guthoff, C. Kleinwort, R. Mankel, H. Maser, C. Muhl, A. Mussgiller, A. Nürnberg, Y. Otarid, D. Perez Adan, H. Petersen, D. Pitzl, D. Rastorguev, O. Reichelt, P. Schütze, L. Sreelatha Pramod, R. Stever, A. Velyka, A. Ventura Barroso, R. Walsh, A. Zuber

University of Hamburg, Hamburg, Germany
A. Albrecht, M. Antonello, H. Biskop, P. Buhmann, P. Connor, F. Feindt[6], E. Garutti, M. Hajheidari[7], J. Haller, A. Hinzmann[6], H. Jabusch, G. Kasieczka, R. Klanner, V. Kutzner, J. Lange, S. Martens, M. Mrowietz, Y. Nissan, K. Pena, B. Raciti, P. Schleper, J. Schwandt, G. Steinbrück*, A. Tews, J. Wellhausen

Institut für Experimentelle Teilchenphysik, KIT, Karlsruhe, Germany
L. Ardila[8], M. Balzer[8], T. Barvich, B. Berger, E. Butz, M. Caselle[8], A. Dierlamm[8], U. Elicabuk, M. Fuchs[8], F. Hartmann, U. Husemann, G. Kösker, R. Koppenhöfer, S. Maier, S. Mallows, T. Mehner[8], Th. Muller, M. Neufeld, O. Sander[8], I. Shvetsov, H. J. Simonis, P. Steck, L. Stockmeier, B. Topko, F. Wittig

Institute of Nuclear and Particle Physics (INPP), NCSR Demokritos, Aghia Paraskevi, Greece
G. Anagnostou, P. Assiouras, G. Daskalakis, I. Kazas, A. Kyriakis, D. Loukas

Wigner Research Centre for Physics, Budapest, Hungary
T. Balázs, M. Bartók, K. Márton, F. Siklér, V. Veszprémi

National Institute of Science Education and Research, HBNI, Bhubaneswar, India
S. Bahinipati[9], A.K. Das, P. Mal, A. Nayak[10], D.K. Pattanaik, P. Saha, S.K. Swain

University of Delhi, Delhi, India
A. Bhardwaj, C. Jain, A. Kumar, T. Kumar, K. Ranjan, S. Saumya

Saha Institute of Nuclear Physics, HBNI, Kolkata, India
S. Baradia, S. Dutta, P. Palit, G. Saha, S. Sarkar

Indian Institute of Technology Madras, Madras, India
M. Alibordi, P.K. Behera, S.C. Behera, S. Chatterjee, G. Dash, P. Jana, P. Kalbhor, J. Libby, M. Mohammad, R. Pradhan, P.R. Pujahari, N.R. Saha, K. Samadhan, A. Sharma, A.K. Sikdar, R. Singh, S. Verma, A. Vijay

INFN Sezione di Bari[a], Università di Bari[b], Politecnico di Bari[c], Bari, Italy
P. Cariola[a], D. Creanza[a,c], M. de Palma[a,b], G. De Robertis[a], A. Di Florio[a,c], L. Fiore[a], F. Loddo[a], I. Margjeka[a], M. Mongelli[a], S. My[a,b], L. Silvestris[a]

INFN Sezione di Catania[a], Università di Catania[b], Catania, Italy
S. Albergo[a,b], S. Costa[a,b], A. Di Mattia[a], R. Potenza[a,b], A. Tricomi[a,b], C. Tuve[a,b]

2023 JINST 18 P11015

INFN Sezione di Firenze[a], Università di Firenze[b], Firenze, Italy
G. Barbagli[a], G. Bardelli[a,b], M. Brianzi[a], B. Camaiani[a,b], A. Cassese[a], R. Ceccarelli[a,b], R. Ciaranfi[a], V. Ciulli[a,b], C. Civinini[a], R. D'Alessandro[a,b], E. Focardi[a,b], T. Kello[a], G. Latino[a,b], P. Lenzi[a,b], M. Lizzo[a,b], M. Meschini[a], S. Paoletti[a], A. Papanastassiou[a,b], G. Sguazzoni[a], L. Viliani[a]

INFN Sezione di Genova, Genova, Italy
S. Cerchi, F. Ferro, S. Minutoli, E. Robutti

INFN Sezione di Milano-Bicocca[a], Università di Milano-Bicocca[b], Milano, Italy
F. Brivio[a], M.E. Dinardo[a,b], P. Dini[a], S. Gennai[a], L. Guzzi[a,b], S. Malvezzi[a], D. Menasce[a], L. Moroni[a], D. Pedrini[a], D. Zuolo[a,b]

INFN Sezione di Padova[a], Università di Padova[b], Padova, Italy
P. Azzi[a], N. Bacchetta[a], P. Bortignon[a,11], D. Bisello[a], T.Dorigo[a], E. Lusiani[a], M. Tosi[a,b]

INFN Sezione di Pavia[a], Università di Bergamo[b], Bergamo, Università di Pavia[c], Pavia, Italy
L. Gaioni[a,b], M. Manghisoni[a,b], L. Ratti[a,c], V. Re[a,b], E. Riceputi[a,b], G. Traversi[a,b]

INFN Sezione di Perugia[a], Università di Perugia[b], CNR-IOM Perugia[c], Perugia, Italy
P. Asenov[a,c], G. Baldinelli[a,b], F. Bianchi[a,b], G.M. Bilei[a], S. Bizzaglia[a], M. Caprai[a], B. Checcucci[a], D. Ciangottini[a], A. Di Chiaro[a], L. Fanò[a,b], L. Farnesini[a], M. Ionica[a], M. Magherini[a,b], G. Mantovani[a,b], V. Mariani[a,b], M. Menichelli[a], A. Morozzi[a], F. Moscatelli[a,c], D. Passeri[a,b], A. Piccinelli[a,b], P. Placidi[a,b], A. Rossi[a,b], A. Santocchia[a,b], D. Spiga[a], L. Storchi[a], T. Tedeschi[a,b], C. Turrioni[a,b]

INFN Sezione di Pisa[a], Università di Pisa[b], Scuola Normale Superiore di Pisa[c], Pisa, Italy, Università di Siena[d], Siena, Italy
P. Azzurri[a], G. Bagliesi[a], A. Basti[a,b], R. Battacharya[a], R. Beccherle[a], D. Benvenuti[a], L. Bianchini[a,b], T. Boccali[a], F. Bosi[a], D. Bruschini[a,c], R. Castaldi[a], M.A. Ciocci[a,b], V. D'Amante[a,d], R. Dell'Orso[a], S. Donato[a], A. Giassi[a], F. Ligabue[a,c], G. Magazzù[a], M. Massa[a], E. Mazzoni[a], A. Messineo[a,b], A. Moggi[a], M. Musich[a,b], F. Palla[a], S. Parolia[a], P. Prosperi[a], F. Raffaelli[a], G. Ramirez Sanchez[a,c], A. Rizzi[a,b], S. Roy Chowdhury[a], T. Sarkar[a], P. Spagnolo[a], R. Tenchini[a], G. Tonelli[a,b], A. Venturi[a], P.G. Verdini[a]

INFN Sezione di Torino[a], Università di Torino[b], Torino, Italy
N. Bartosik[a], R. Bellan[a,b], S. Coli[a], M. Costa[a,b], R. Covarelli[a,b], G. Dellacasa[a], N. Demaria[a], S. Garbolino[a], S. Garrafa Botta[a], M. Grippo[a,b], F. Luongo[a,b], A. Mecca[a,b], E. Migliore[a,b], G. Ortona[a], L. Pacher[a,b], F. Rotondo[a], A. Solano[a,b], C. Tarricone[a,b], A. Vagnerini[a,b]

National Centre for Physics, Islamabad, Pakistan
A. Ahmad, M.I. Asghar, A. Awais, M.I.M. Awan, M. Saleh

Instituto de Física de Cantabria (IFCA), CSIC-Universidad de Cantabria, Santander, Spain
A. Calderón, J. Duarte Campderros, M. Fernandez, G. Gomez, F.J. Gonzalez Sanchez, R. Jaramillo Echeverria, C. Lasaosa, D. Moya, J. Piedra, A. Ruiz Jimeno, L. Scodellaro, I. Vila, A.L. Virto, J.M. Vizan Garcia

2023 JINST 18 P11015

CERN, European Organization for Nuclear Research, Geneva, Switzerland

D. Abbaneo, M. Abbas, I. Ahmed, E. Albert, B. Allongue, J. Almeida, M. Barinoff, J. Batista Lopes, G. Bergamin[12], G. Blanchot, F. Boyer, A. Caratelli, R. Carnesecchi, D. Ceresa, J. Christiansen, J. Daguin, A. Diamantis, M. Dudek, F. Faccio, N. Frank, T. French, D. Golyzniak, J. Kaplon, K. Kloukinas, N. Koss, L. Kottelat, M. Kovacs, J. Lalic, A. La Rosa, P. Lenoir, R. Loos, A. Marchioro, A. Mastronikolis, I. Mateos Dominguez[13], S. Mersi, S. Michelis, C. Nedergaard, A. Onnela, S. Orfanelli, T. Pakulski, A. Papadopoulos[14], F. Perea Albela, A. Perez, F. Perez Gomez, J.-F. Pernot, P. Petagna, Q. Piazza, G. Robin, S. Scarfì[15], K. Schleidweiler, N. Siegrist, M. Sinani, P. Szidlik, P. Tropea, J. Troska, A. Tsirou, F. Vasey, R. Vrancianu, S. Wlodarczyk, A. Zografos[16]

Paul Scherrer Institut, Villigen, Switzerland

W. Bertl[†], T. Bevilacqua[17], L. Caminada[17], A. Ebrahimi, W. Erdmann, R. Horisberger, H.-C. Kaestli, D. Kotlinski, C. Lange, U. Langenegger, B. Meier, M. Missiroli[17], L. Noehte[17], T. Rohe, S. Streuli

Institute for Particle Physics and Astrophysics, ETH Zurich, Zurich, Switzerland

K. Androsov, M. Backhaus, R. Becker, G. Bonomelli, D. di Calafiori, A. Calandri, A. de Cosa, M. Donega, F. Eble, F. Glessgen, C. Grab, T. Harte, D. Hits, W. Lustermann, J. Niedziela, V. Perovic, M. Reichmann, B. Ristic, U. Roeser, D. Ruini, R. Seidita, J. Sörensen, R. Wallny

Universität Zürich, Zurich, Switzerland

P. Bärtschi, K. Bösiger, F. Canelli, K. Cormier, A. De Wit, M. Huwiler, W. Jin, A. Jofrehei, B. Kilminster, S. Leontsinis, S.P. Liechti, A. Macchiolo, R. Maier, U. Molinatti, I. Neutelings, A. Reimers, P. Robmann, S. Sanchez Cruz, Y. Takahashi, D. Wolf

National Taiwan University (NTU), Taipei, Taiwan

P.-H. Chen, W.-S. Hou, R.-S. Lu

University of Bristol, Bristol, United Kingdom

E. Clement, D. Cussans, J. Goldstein, S. Seif El Nasr-Storey, N. Stylianou, K. Walkingshaw Pass

Rutherford Appleton Laboratory, Didcot, United Kingdom

K. Harder, M.-L. Holmberg, K. Manolopoulos, T. Schuh, I.R. Tomalin

Imperial College, London, United Kingdom

R. Bainbridge, C. Brown, G. Fedi, G. Hall, D. Monk, D. Parker, M. Pesaresi, K. Uchida

Brunel University, Uxbridge, United Kingdom

K. Coldham, J. Cole, M. Ghorbani, A. Khan, P. Kyberd, I.D. Reid

The Catholic University of America, Washington DC, U.S.A.

R. Bartek, A. Dominguez, C. Huerta Escamilla, R. Uniyal, A.M. Vargas Hernandez

Brown University, Providence, U.S.A.

G. Benelli, X. Coubez, U. Heintz, N. Hinton, J. Hogan[18], A. Honma, A. Korotkov, D. Li, J. Luo, M. Narain[†], N. Pervan, T. Russell, S. Sagir[19], F. Simpson, E. Spencer, C. Tiley, P. Wagenknecht

2023 JINST 18 P11015

University of California, Davis, Davis, U.S.A.
E. Cannaert, M. Chertok, J. Conway, D. Hemer, F. Jensen, J. Thomson, W. Wei, T. Welton, F. Zhang

University of California, Riverside, Riverside, U.S.A.
G. Hanson

University of California, San Diego, La Jolla, U.S.A.
S.B. Cooperstein, R. Gerosa, L. Giannini, Y. Gu, S. Krutelyov, B.N. Sathia, V. Sharma, M. Tadel, E. Vourliotis, A. Yagil

University of California, Santa Barbara - Department of Physics, Santa Barbara, U.S.A.
J. Incandela, S. Kyre, P. Masterson

University of Colorado Boulder, Boulder, U.S.A.
J.P. Cumalat, W.T. Ford, A. Hassani, M. Herrmann, G. Karathanasis, F. Marini, C. Savard, N. Schonbeck, K. Stenson, K.A. Ulmer, S.R. Wagner, N. Zipper

Cornell University, Ithaca, U.S.A.
J. Alexander, S. Bright-Thonney, X. Chen, D. Cranshaw, A. Duquette, J. Fan, X. Fan, A. Filenius, D. Gadkari, J. Grassi, S. Hogan, P. Kotamnives, S. Lantz, J. Monroy, G. Niendorf, H. Postema, J. Reichert, M. Reid, D. Riley, A. Ryd, K. Smolenski, C. Strohman, J. Thom, P. Wittich, R. Zou

Fermi National Accelerator Laboratory, Batavia, U.S.A.
A. Bakshi, D.R. Berry, K. Burkett, D. Butler, A. Canepa, G. Derylo, J. Dickinson, A. Ghosh, H. Gonzalez, S. Grünendahl, L. Horyn, M. Johnson, P. Klabbers, C.M. Lei, R. Lipton, S. Los, P. Merkel, S. Nahn, F. Ravera, L. Ristori, R. Rivera, L. Spiegel, L. Uplegger, E. Voirin, I. Zoi

Florida State University, Tallahassee, U.S.A.
S. Bower, R. Habibullah, M. Wulansatiti, R. Yohay

University of Illinois at Chicago (UIC), Chicago, U.S.A.
S. Dittmer, R. Escobar Franco, A. Evdokimov, O. Evdokimov, C.E. Gerber, M. Hawksworth, D.J. Hofman, C. Mills, B. Ozek, T. Roy, S. Rudrabhatla, J. Yoo

The University of Iowa, Iowa City, U.S.A.
M. Alhusseini, D. Blend, T. Bruner, M. Haag, J. Nachtman, Y. Onel, C. Snyder, K. Yi[20]

Johns Hopkins University, Baltimore, U.S.A.
J. Davis, A.V. Gritsan, L. Kang, S. Kyriacou, P. Maksimovic, M. Roguljic, S. Sekhar, M. Swartz, T. Vami

The University of Kansas, Lawrence, U.S.A.
J. Anguiano, A. Bean, D. Grove, R. Salvatico, C. Smith, G. Wilson

Kansas State University, Manhattan, U.S.A.
A. Ivanov, A. Kalogeropoulos, G. Reddy, R. Taylor

2023 JINST 18 P11015

University of Nebraska-Lincoln, Lincoln, U.S.A.
K. Bloom, D.R. Claes, C. Fangmeier, F. Golf, G. Haza, C. Joo, I. Kravchenko, J. Siado

State University of New York at Buffalo, Buffalo, U.S.A.
I. Iashvili, A. Kharchilava, D. Nguyen, J. Pekkanen, S. Rappoccio

Boston University, Boston, U.S.A.
A. Akpinar, Z. Demiragli, D. Gastler, P. Gkountoumis, E. Hazen, A. Peck, J. Rohlf

Northeastern University, Boston, U.S.A.
J. Li, A. Parker, L. Skinnari

Northwestern University, Evanston, U.S.A.
K. Hahn, Y. Liu, S. Noorudhin

The Ohio State University, Columbus, U.S.A.
A. Basnet, C.S. Hill, M. Joyce, K. Wei, B. Winer, B. Yates

University of Puerto Rico, Mayaguez, U.S.A.
S. Malik

Purdue University, West Lafayette, U.S.A.
R. Chawla, S. Das, M. Jones, A. Jung, A. Koshy, M. Liu, G. Negro, J. Thieman

Purdue University Northwest, Hammond, U.S.A.
J. Dolen, N. Parashar, A. Pathak

Rice University, Houston, U.S.A.
K.M. Ecklund, S. Freed, A. Kumar, T. Nussbaum

University of Rochester, Rochester, U.S.A.
R. Demina, J. Dulemba, O. Hindrichs

Rutgers, The State University of New Jersey, Piscataway, U.S.A.
Y. Gershtein, E. Halkiadakis, A. Hart, C. Kurup, A. Lath, K. Nash, M. Osherson, S. Schnetzer, R. Stone

University of Tennessee, Knoxville, U.S.A.
D. Ally, S. Fiorendi, J. Harris, T. Holmes, L. Lee, E. Nibigira, S. Spanier

Texas A&M University, College Station, U.S.A.
R. Eusebi

Vanderbilt University, Nashville, U.S.A.
P. D'Angelo, W. Johns

[*] *Corresponding author*
[†] *Deceased*

2023 JINST 18 P11015

[1] *Also at Vienna University of Technology, Vienna, Austria*
[2] *Also at Institute of Basic and Applied Sciences, Faculty of Engineering, Arab Academy for Science, Technology and Maritime Transport, Alexandria, Egypt*
[3] *Also at Vrije Universiteit Brussel (VUB), Brussel, Belgium*
[4] *Also at Université de Haute-Alsace, Mulhouse, France*
[5] *Also at University of Hamburg, Hamburg, Germany*
[6] *Now at Deutsches Elektronen-Synchrotron, Hamburg, Germany*
[7] *Now at CERN, European Organization for Nuclear Research, Geneva, Switzerland*
[8] *Also at Institute for Data Processing and Electronics, KIT, Karlsruhe, Germany*
[9] *Also at Indian Institute of Technology, Bhubaneswar, India*
[10] *Also at Institute of Physics, HBNI, Bhubaneswar, India*
[11] *Also at University of Cagliari, Cagliari, Italy*
[12] *Also at Institut Polytechnique de Grenoble, Grenoble, France*
[13] *Also at Universidad de Castilla-La-Mancha, Ciudad Real, Spain*
[14] *Also at University of Patras, Patras, Greece*
[15] *Also at École Polytechnique Fédérale de Lausanne, Lausanne, Switzerland*
[16] *Also at National Technical University of Athens, Athens, Greece*
[17] *Also at Universität Zürich, Zurich, Switzerland*
[18] *Now at Bethel University, St. Paul, Minnesota, U.S.A.*
[19] *Now at Karamanoglu Mehmetbey University, Karaman, Turkey*
[20] *Also at Nanjing Normal University, Nanjing, China*

2023 JINST 18 P11015